HiSST: International Conference on
High-Speed Vehicle Science & Technology
26–29 November 2018, Moscow, Russia

HIGH AND LOW SPEED ANALYSIS OF A RE-USABLE UNMANNED RE-ENTRY VEHICLE

Tamás Bykerk [1], Giuseppe Pezzella [2], Antonio Viviani [3] and Dries Verstraete [1]

Abstract

Re-usable, unmanned re-entry vehicles are an efficient way to experimentally validate next generation re-entry technologies. During the descent phase, the aircraft will encounter free-stream velocities ranging from hypersonic to low subsonic, which requires a careful choice of aeroshape. For the mission to be successful, the vehicle will need to be stable during both low and high-speed phases of flight. In this framework, the paper focused attention on both experimental and numerical flowfield investigations carried out on an innovative spatuled-body vehicle aeroshape. Wind tunnel results from a low speed test campaign performed in order to validate subsonic CFD studies are provided and discussed in the paper. Results of Mach 7 CFD simulations are also shown to understand the high-speed behavior of the aircraft. Findings of this study show that the vehicle requires a MRC location at 45% of its length for static stability at both high and low speed. Control deflection studies showed that the first estimate of elevon sizing is sufficient and the aircraft can easily be trimmed at both high and low speed.

Keywords: *Subsonic, Hypersonic, CFD, Static Stability, Wind Tunnel Testing, Re-entry flying test bed.*

Nomenclature

AoA – Angle of Attack
AoA – Angle of Sideslip
CFD – Computational Fluid Dynamics
C_A – Axial force coefficient
C_D – Drag force coefficient
C_L – Lift force coefficient
Cl, CLL – Rolling moment coefficient
Cm, CM – Pitching moment coefficient
Cn, CLN – Yawing moment coefficient
C_Y – Side force coefficient
D – Drag force
H – Altitude
L/D – Aerodynamic efficiency
L – Lift force
M – Mach number
MRC – Moment Reference Centre
P - Pressure
RANS – Reynolds Average Navier-Stokes Eqs.
Re – Reynolds number
T – Temperature
WT – Wind Tunnel
WTT – Wind Tunnel Tests

α – Angle of attack
β – Angle of sideslip
δ – Generic control deflection
δ_e – Elevons deflection angle

Subscripts
left – left aileron deflection
right – right aileron deflection
∞ - free-stream conditions

[1] *School of Aerospace, Mechanical and Mechatronic Engineering, Building J07, Maze Crescent, Darlington Campus, University of Sydney, NSW 2006, Australia, tamas.bykerk@sydney.edu.au, dries.verstraete@sydney.edu.au*
[2] *Italian Aerospace Research Centre, CIRA. Analysis and Extrapolation to Flight Lab. Head. g.pezzella@cira.it.*
[3] *University of Campania, Engineering Department. Chair of Fluid Dynamics. antonio.viviani@unicampania.it*

1. Introduction

Re-usable vehicles are often favored over their single use counterparts for enabling quicker launch turnaround times as well as introducing sustainability to flight programs. During the design life cycle of these vehicles, the "per launch" cost is significantly lowered as the complete vehicle is recovered, refurbished and reused.

The vehicle presented here will be a test-bed for new re-entry technologies such as thermal protection systems. In this framework, a lifting-body aeroshape with a double-delta planform wing and V-tail vertical planes was chosen and its aerodynamic performance were investigated both at numerical and experimental level [1-2].

The vehicle, shown in Fig 1, has been developed by the Italian Aerospace Research Centre (CIRA) in the framework of its past Unmanned Space Vehicle (USV) program [2].

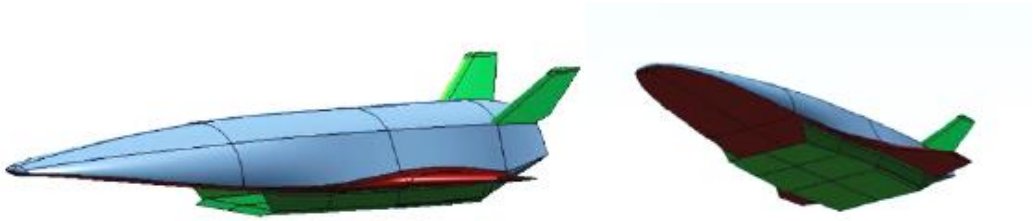

Fig 1. CIRA V-One Vehicle.

This test-bed, named V-one (i.e., first version), is a re-entry space glider characterized by a relatively simple, spatuled-body architecture, able to validate hypersonic aerothermodynamic design databases and passenger experiments, including thermal shield and hot structures, giving confidence that a full-scale development can successfully proceed. As shown in Fig 1, the vehicle features an integrated scramjet pod located on the underside of the body. However, in the present research effort, the external scramjet pod has been removed and the three-view of the investigated aeroshape can be seen in Fig 2.

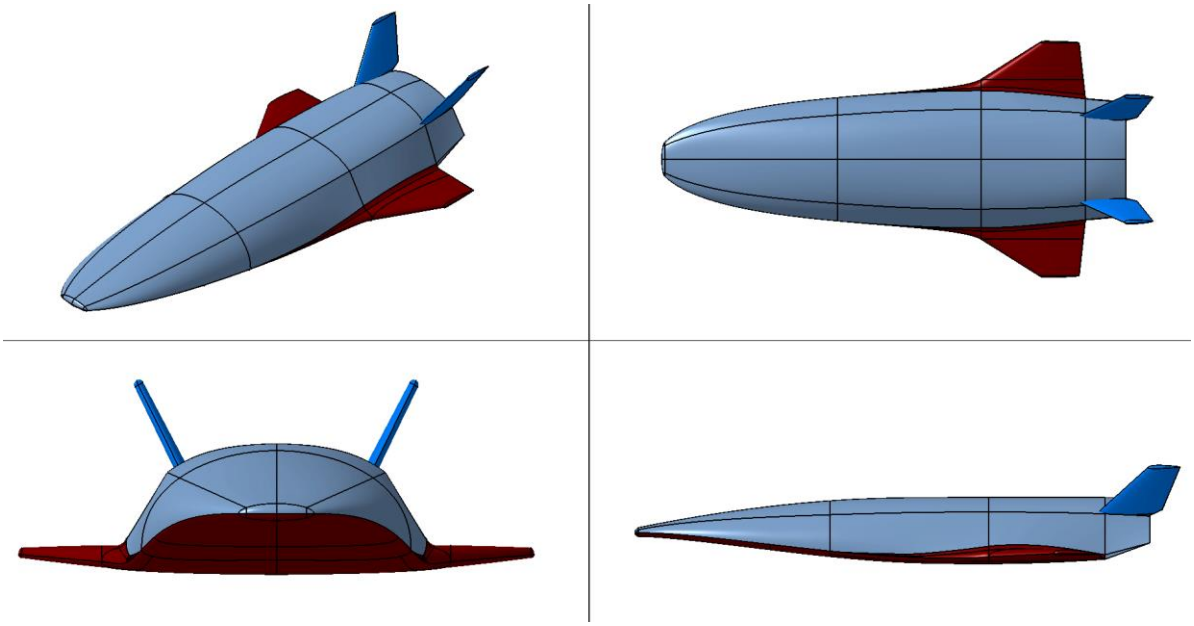

Fig 2. Three-view vehicle.

A preliminary elevon dimensioning is also addressed, as shown in Fig 3. The vertical tail was assumed fully movable (i.e., ruddervator).

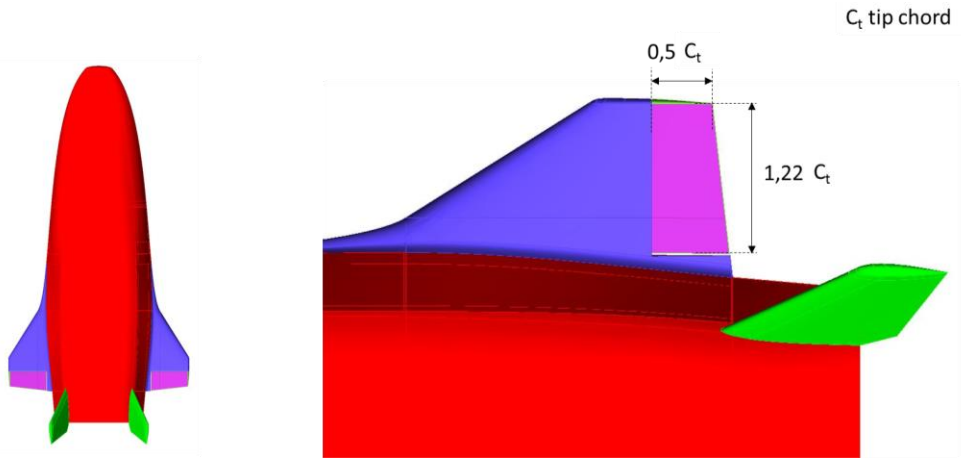

Fig 3. Vehicle elevon dimensions.

This paper discusses results from low and high-speed aerodynamic analysis using both Wind tunnel (WT) and Computational Fluid Dynamics (CFD) investigations. First, a Mach 7 and 30 Km altitude design point study is presented since this flight condition is representative of hypersonic cruise conditions of a scramjet propelled aircraft. Then, results from the low-speed analysis are compared with wind tunnel tests at the same condition in order to validate the modelling methods. All cases analyze the vehicle through a range of control deflections, angle of attack (AoA) and angle of sideslip (AoS). This data is used to extract aerodynamic coefficients for a performance analysis as well as static stability derivatives.

2. Methodology

The paper addresses both experimental and numerical flowfield investigations of the V-one aeroshape. WT results refers to a low speed test campaign carried out at the University of Sydney. On the other hand, vehicle aerodynamics is also addressed through CFD simulations performed at both low and high-speed conditions. Therefore, results for subsonic flow from both WT and CFD are available; while at hypersonic flow only CFD investigations exist.

Finally, local surface inclination methods (i.e., Newtonian panel method) are applied to preliminarily explore vehicle aerodynamics at hypersonic speed flow conditions. In fact, every lay-out deemed as infeasible by the preliminary aerodynamic examination has no reasonable chance of realization. Therefore, the approach implemented in the engineering-based approach is fully justified as it is much easier and more rapid to operate, and hence the assessment of configuration changes can be done extremely fast.

2.1. Low Speed Wind Tunnel Testing

The wind tunnel test campaign was completed in the 7 x 5 foot low-speed facility at the University of Sydney. The model was fabricated using an assembly of 3D printed pieces, which were then glued together and sanded for a smooth finish. Components such as the wings and fins are removable to allow the testing of various control settings. The model measurements are summarized in Table 1.

Table 1. Summary of wind tunnel model geometry

Parameter	Description	Value	Units
L_{ref}	Vehicle body length	0.662	m
S_{ref}	Vehicle body wetted area	0.129	m^2
b_{ref}	Vehicle wingspan length	0.33	m

Load cell measurements were taken in the body axis at 30 m/s through a range of AoA and AoS to determine aerodynamic and static stability derivatives for a clean configuration (i.e., no aerodynamic surfaces deflected). The load cell was enclosed within the body of the model to minimize the effect of the sting on the measurements. The model can be seen mounted in the wind tunnel in Fig 4.

Fig 4. Views of model in wind tunnel.

2.2. Low Speed Performance and Flowfield Numerical Investigations

For the low-speed investigations, the Reynolds number of the CFD has been set to match the wind tunnel tests to allow a fair comparison of data. The SST k-ω turbulence model was used for its ability to model separated flows and regions of circulation. The steady state, pressure based coupled solver in ANSYS FLUENT® was used for all subsonic simulations.

The low speed mesh setup is shown in Fig 5. The mesh is comprised of unstructured elements with prism inflation layers for the boundary layer discretization (Y^+=O(1) at wall). As shown, the grid features a body of influence surrounding the vehicle for mesh refinement. The domain extends approximately 15 chord lengths upstream and 25 downstream. For longitudinal simulations, a symmetry boundary condition is used to lower computation time, with the half body mesh comprising of about 7M cells. A full body mesh is required for sideslip calculations with approximately double the amount of elements.

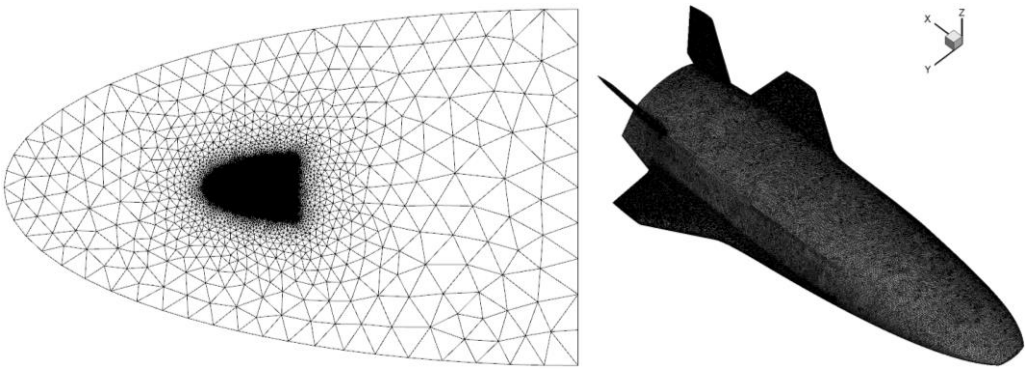

Fig 5. Low Speed CFD Domain (unstructured grid) and vehicle surface Mesh.

A structured low speed grid has been also generated in order to address a sensitivity analysis about unstructured versus structured grid results. The mesh, generated by using ICEMCFD® software, is shown in Fig 6. This multiblock structured grid features 51 blocks for about 7M cells (half body).

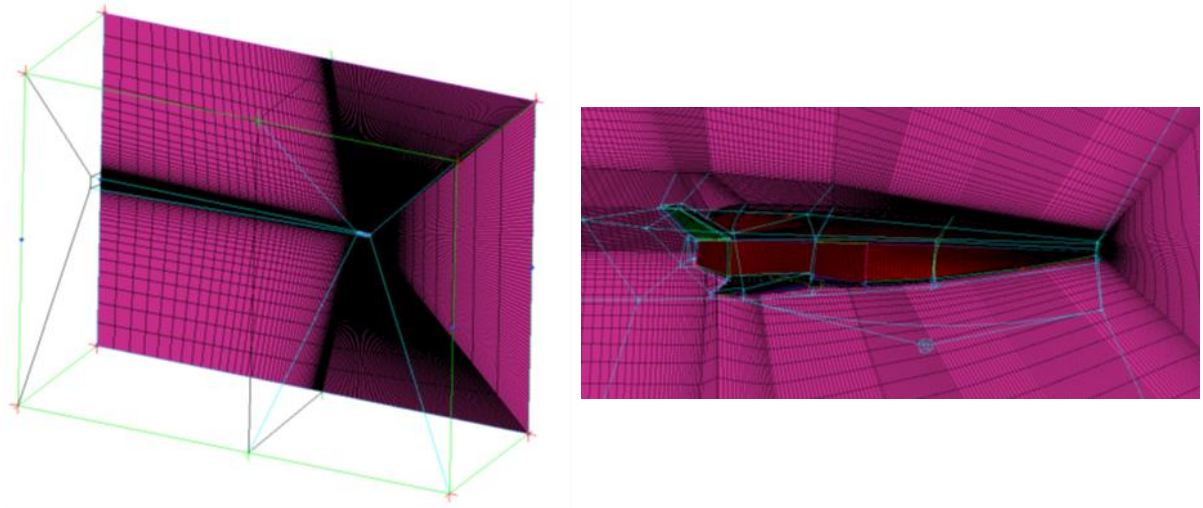

Fig 6. Low speed structured grid and vehicle surface mesh.

2.3. High-Speed Performance and Flowfield Numerical Investigations

Preliminary assessment of aircraft aerodynamics was extensively performed by using a 3D Panel Method code developed by CIRA (SIM–Surface Impact Method) in the frame of its research activities on preliminary design of a re-entry vehicle. This tool at high supersonic and hypersonic speeds is able to accomplish the aerodynamic and aero-thermodynamic analyses of a complex arbitrary three-dimensional re-entry vehicle configuration by using simplified approaches as local surface inclination methods and approximate boundary-layer methods respectively, thus avoiding the time consuming and complex grid generation and computation processes of CFD.

Generally speaking, SIM gives good results for longitudinal aerodynamic coefficients at supersonic and, especially, at hypersonic speeds. The reliability of SIM estimations within free-molecular flow regime conditions has been also highlighted. The SIM predictions of lateral/directional aerodynamic coefficients are of the first order accuracy. The side force and rolling moment coefficient predictions are satisfactory for wing-body type configurations. However, the yawing moment coefficient is susceptible to error, especially for body dominated configurations. An example of surface panel mesh considered for the Newtonian aerodynamics assessment of aircraft in shown in Fig 7.

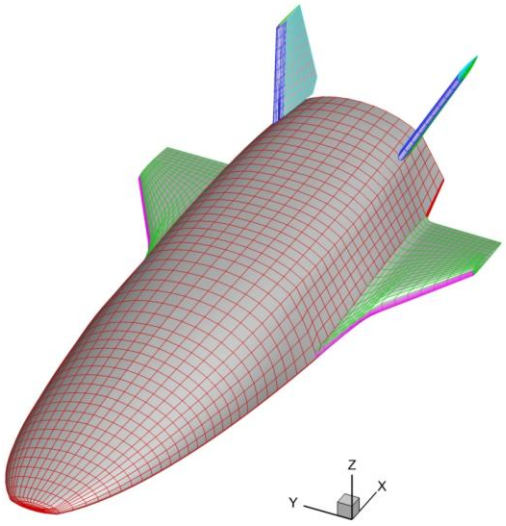

Fig 7. Surface panel mesh.

As shown, the vehicle surface is approximated by a system of planar panels; the lowest level of geometry used in the analysis is a quadrilateral element. The pressure acting on each panel is evaluated by user-specified compression-expansion and approximate boundary-layer methods. The methods to be used in calculating the pressure in impact and shadow regions may be specified independently and

can be selected by the user. In the present analysis, modified Newtonian theory and tangent cone/wedge methods are widely applied. The different parts of the vehicle (fuselage, wing and vertical tail) are analyzed separately, and global vehicle aerodynamic coefficients are obtained by appropriate summation of component contributions (i.e., build-up approach).

Numerical flowfield investigations are performed with the commercial CFD code ANSYS FLUENT®. The Reynolds Averaged Navier-Stokes (RANS) equations are integrated by means of the finite volume approach. The Flux Difference Splitting (FDS) second-order upwind scheme (least square cell based) has been used for the spatial reconstruction of convective terms, while for the diffusive fluxes a cell-centred scheme has been applied. An implicit scheme has been considered for time integration; while flow turbulence effects were simulated through the K-ω SST turbulence model applied to a steady state solution. The ideal gas model for air was assumed for both low and high-speed computations. Note that, even though CFD simulations have been carried out at hypersonic flow conditions, the ideal gas assumption was still valid. The reason is that the aeroshape features a very slender configuration and shall fly at rather low angle of attack (i.e., weak attached shock waves).

A temperature-dependent formulation was considered for the specific heat at constant pressure c_p (i.e., thermally perfect gas) to accommodate the rather high flow energy [3]. The following polynomial formulation for the c_p was considered:

$$c_p = 5.71\times10^{-18}T^6 - 9.79\times10^{-14}T^5 + 5.22\times10^{-10}T^4$$
$$-1.27\times10^{-6}T^3 + 1.46\times10^{-3}T^2 - 5.46\times10^{-1}T + 1.07\times10^{3}$$

where the flow temperature ranges from 100 K to 2000 K.

For T<100 K c_p=1039.59 [J/kg/K], while for T>2000 K c_p=1265.35 [J/kg/K]. Sutherland's relationship was assumed for the dynamic viscosity. As far as boundary conditions are concerned, the radiative cooled wall (ε=0.8) was assumed for all the flight conditions with the exception of low-speed computations, where a more appropriate boundary condition has been assumed at wall.

A multi-block structured grid was built for high-speed aerodynamic and aerothermodynamic investigations and is shown in Fig 8. The computational domain is tailored for the free-stream conditions of the selected descent flight points. Therefore, for each case a new grid has been created to properly accommodate for the detached bow shock location. The baseline grid topology for this work consists of 51 blocks for an overall number of about 7M cells (half body). Then, the grid is constructed to permit local refinement in order to improve numerical results. In particular, the mesh was initially generated algebraically and then adapted as the solution evolved (i.e., solution adaptive approach), aligning the grid with the bow shock and clustering points in the boundary layer, with the constraint condition of Y^+=O(1) at wall.

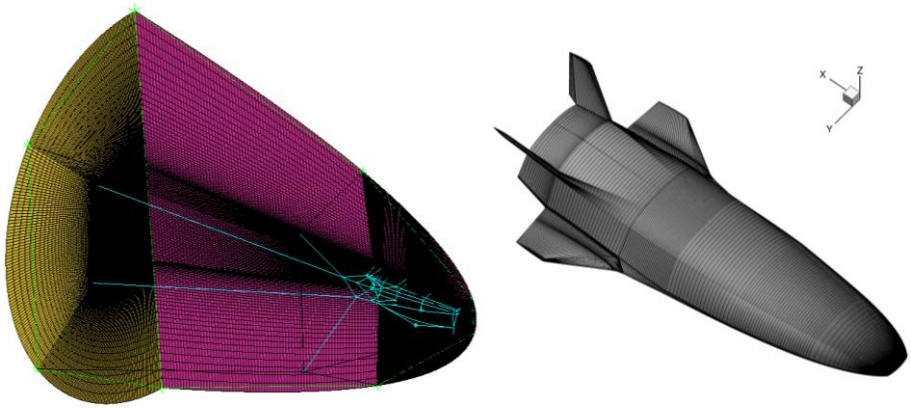

Fig 8. High-speed CFD domain and mesh.

For elevon control authority studies, unstructured hybrid meshes are generated also for hypersonic flow conditions. An example of those meshes is provided in Fig 9 for the case of 10 degrees elevon deflection.

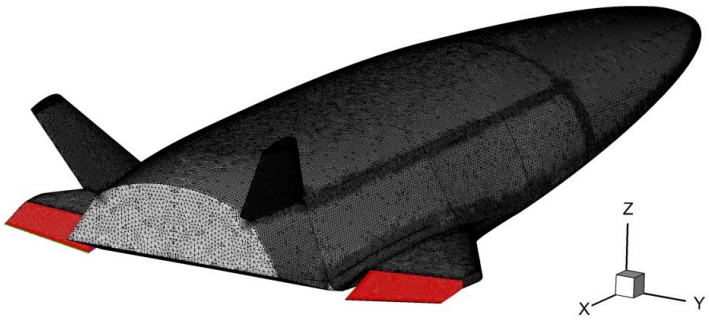

Fig 9. High-speed hybrid mesh for 10 degree elevon deflection.

3. Aerodynamic Results

The vehicle aerodynamic analysis is reported in terms of lift (C_L), drag (C_D), side force (C_Y), rolling moment (Cl), pitching moment (Cm), and yawing moment (Cn) coefficients, which are calculated according to the following equations.

$$C_i = \frac{F_i}{\frac{1}{2}\rho_\infty V_\infty^2 S_{ref}} \quad i = L,D,Y \quad C_l = \frac{M_x}{\frac{1}{2}\rho_\infty V_\infty^2 b_{ref} S_{ref}} \quad C_m = \frac{M_y}{\frac{1}{2}\rho_\infty V_\infty^2 L_{ref} S_{ref}} \quad C_n = \frac{M_z}{\frac{1}{2}\rho_\infty V_\infty^2 b_{ref} S_{ref}}$$

The calculation of the aerodynamic moment coefficients refers to the moment reference centre (MRC), since vehicle's centre of gravity position is not yet frozen. The fuselage length, L_{ref}, the wing-span, b_{ref}, and the vehicle planform area, S_{ref}, are considered as reference parameters to non-dimensionalize aerodynamic forces and moments.

In particular, aircraft aerodynamics is provided according to the ISO-1151 standard. Therefore, the reference system for the aerodynamic data is a body-fixed axis system, as shown in Fig 10. The subscript "b" indicates the Body Reference Frame (BRF), while "w" indicates the Wind Reference Frame (WRF). The coefficients C_L and C_D are provided in the vehicle's WRF, while C_Y, C_l, C_m, and C_n are evaluated in the vehicle's BRF.

The positive directions of the force/moment coefficients as well as angles are shown in Fig 10. Elevon deflection angles (δ_e), which are not shown, are positive when trailing edge is down.

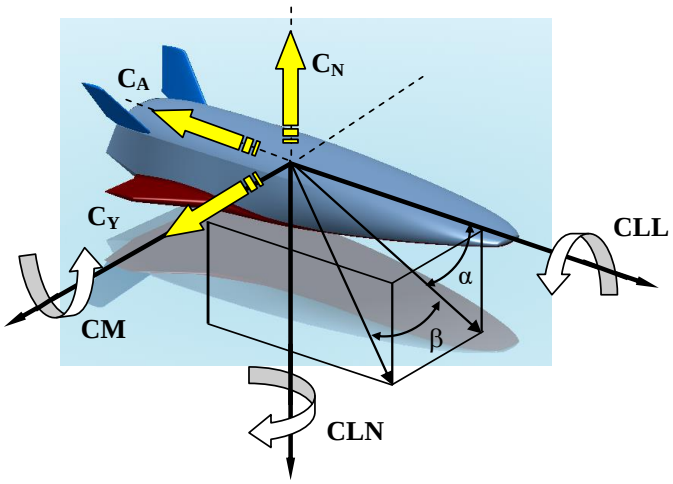

Fig 10. The ISO-1151 standard convention for aerodynamics.

Note that this is the convention usually adopted in Flight Mechanics. As a consequence, the aerodynamic static stability conditions, expressed in terms of derivatives, are the following: $C_{m\alpha}<0$, for longitudinal static stability; and $C_{Y\beta}<0$, $C_{n\beta}>0$, and $C_{l\beta}<0$, for lateral-directional static stability.

Vehicle aerodynamics is provided and discussed hereinafter starting from hypersonic down to subsonic flow conditions, according to a typical re-entry flight.

3.1. High-Speed Aerodynamics

So far, aeroshape high-speed aerodynamics has been assessed at $M_\infty=7$ and 30 Km altitude only ($Re_{Lref}= 12.5x10^6$). This flight condition represents a design point of a scramjet-propelled aircraft in cruise condition and Fig 11 shows the Mach number contours field for 0 degrees AoA. As one can see, the high streamlined sharp leading edges configuration of V-one determines a weak bow shock even though the vehicle is flying at hypersonic conditions. This means that a rather low wave drag component is expected for the aircraft. Note that this represents a figure of particular importance when considering a scramjet-based vehicle configuration.

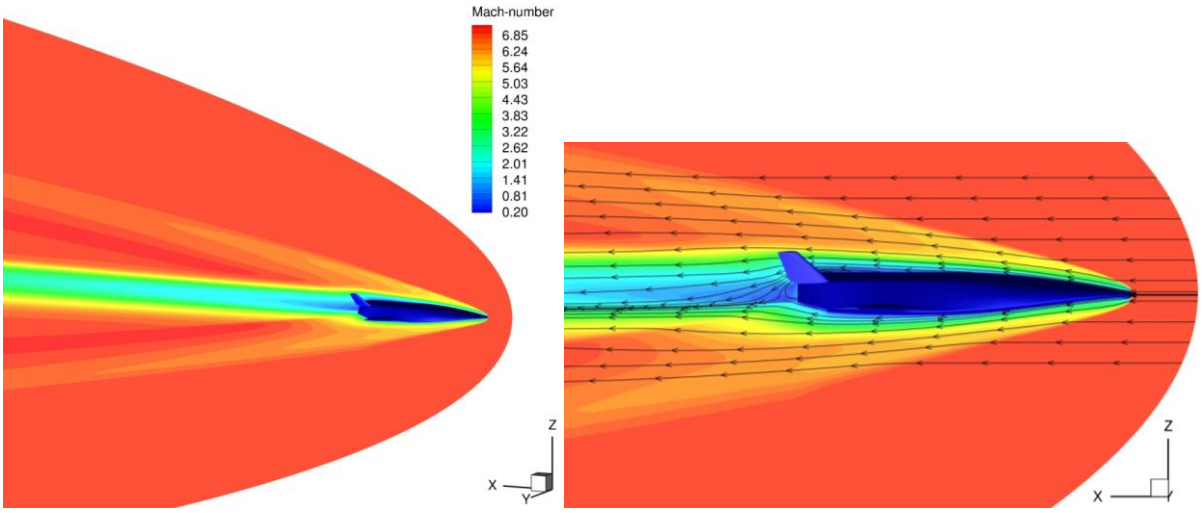

Fig 11. Mach contours field with streamline for $M_\infty=7$ and $\alpha=0$ deg.

The pressure distribution over vehicle surface at $\alpha=0$ deg is provided in Fig 12.

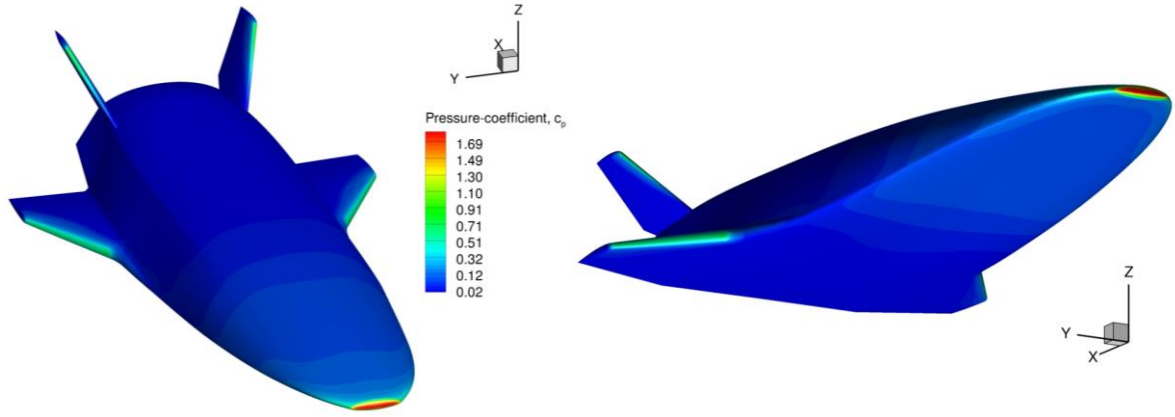

Fig 12. Surface pressure distribution for $M_\infty=7$ and $\alpha=0$ deg.

As expected, aircraft leading edges feature mechanical load overshoots. On those vehicle parts, also large overheating takes place due to sharpness. The equillibrium temperature contours on aircraft surface can be seen in Fig 13, in the case of radiative cooled ($\varepsilon=0.8$) wall boundary condition.

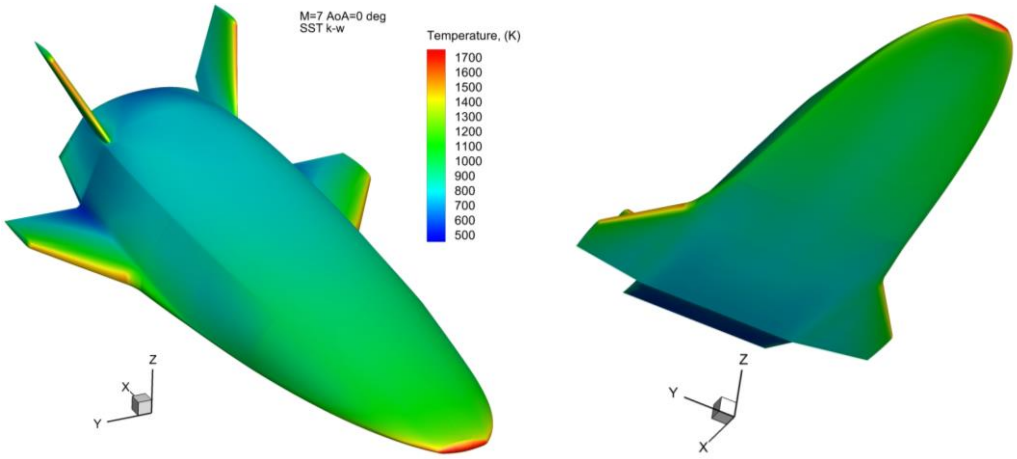

Fig 13. Surface temperature distribution for M_∞=7 and α=0 degrees.

The effects of elevon deflection on vehicle surface temperature distribution at α=0 and 10 degrees for -10°≤δ_{elevon}≤ 10° are shown in Fig 14 and Fig 15. The former provides temperature contours on the aircraft leeside for 0 degrees AoA and δ_{elevon}=-10, 0 and 10 degrees; while the latter figure shows temperature on the vehicle belly side for δ_{elevon}=-10 and 10 degrees. In these figures, skin friction lines are also provided to highlight control surface effectiveness. Indeed, surface streamlines point out that no flow separation is expected at the aileron hinge line for each elevon defection.

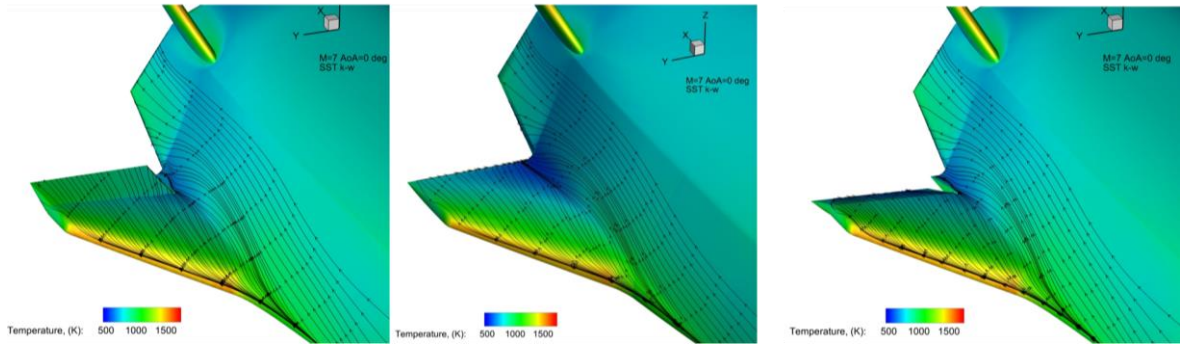

Fig 14. Surface temperature distribution for M_∞=7, α=0 deg and -10°≤δ_{elevon}≤ 10°

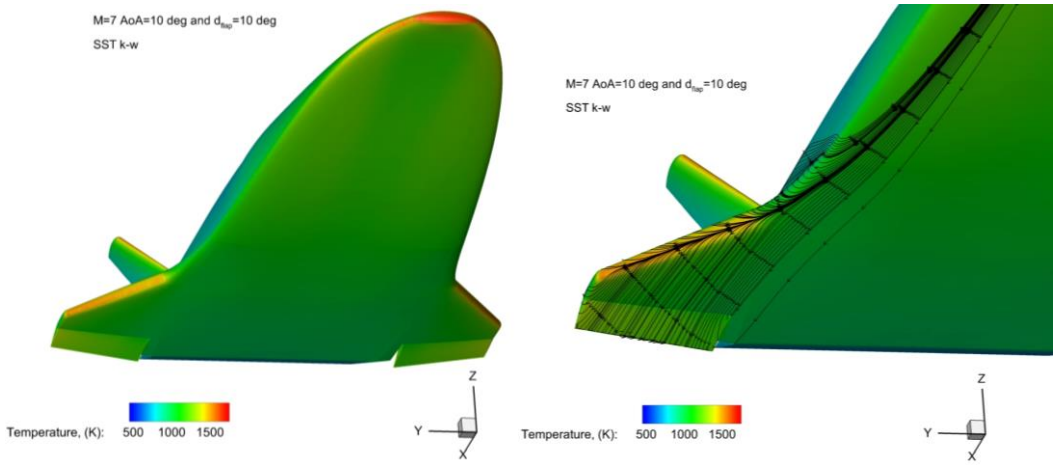

Fig 15. Surface temperature distribution for M_∞=7, α=10 deg and δ_{elevon} =10 deg.

As far as aerodynamic coefficients are concerned, Fig 16 shows the lift, drag, and pitching moment coefficients. The lift-to-drag ratio (L/D) is also presented Fig 16.

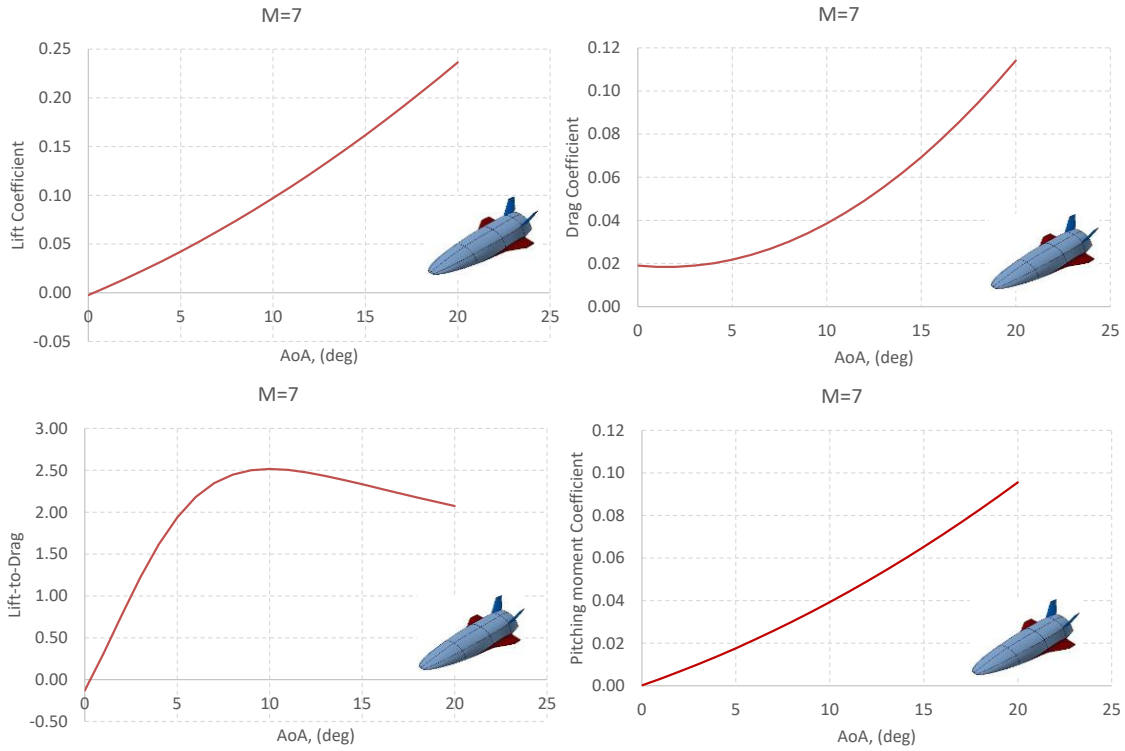

Fig 16. Test-bed clean configuration lift, drag, L/D and pitching moment for M_∞=7 with MRC at 85% L_{ref}.

As one can see, vehicle aerodynamics features a non-linear behavior, as expected for the hypersonic speed flow conditions. The peak aerodynamic efficiency is attained at about 10 degrees AoA. In particular, for the chosen MRC position (85% L_{ref}) the V-one aeroshape resulted in a statically unstable configuration in longitudinal flight conditions. To address this issue, a MRC position sensitivity analysis was performed and the results are found in Fig 17. The effects on the C_m slope of four different MRC positions, namely 48%, 46%, 45%, and 44% L_{ref} are investigated. As shown, in order to have a statically stable configuration the MRC must be shifted forward. Viable options are MRC positions in the range (46÷44) % L_{ref}. In these cases, the aircraft features a natural trim point ranging from about 7 to 3 degrees AoA.

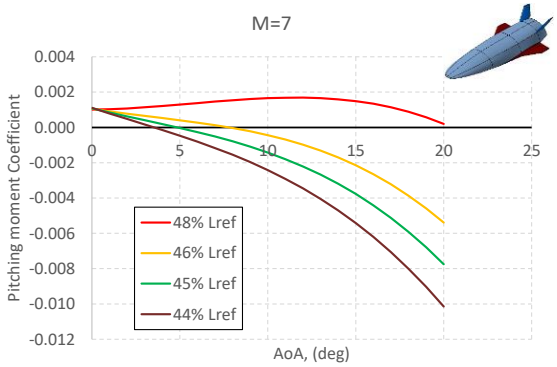

Fig 17. MRC position sensitivity analysis for longitudinal aerodynamics at M_∞=7.

The effect of sideslip flows on aircraft aerodynamics can be seen in Fig 18. These figures point out that V-one is statically unstable in lateral-direction flight conditions for MRC at 85% L_{ref}. This is demonstrated by $C_{Y\beta}<0$, $C_{l\beta}<0$ (only at α=10 deg) but $C_{n\beta}$ is always negative.

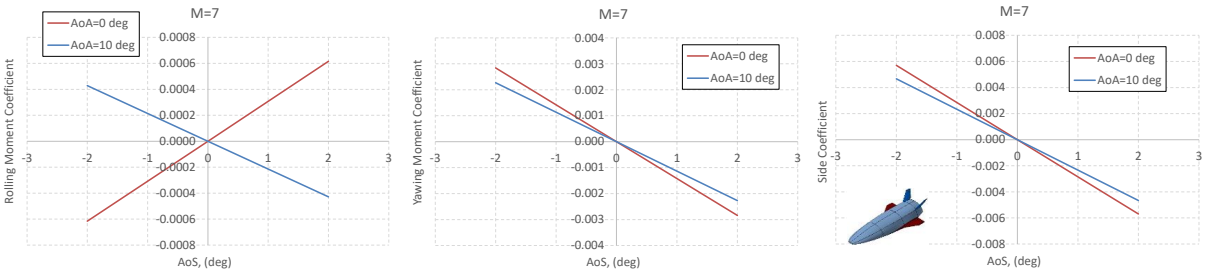

Fig 18. Sideslip aerodynamics for M_∞=7. MRC at 85% L_{ref}.

If the MRC is shifted forward to 45%L_{ref}, $C_{n\beta}$ changes according to Fig 19. At this new location the aeroshape is statically stable both laterally and directionally at 10 deg AoA.

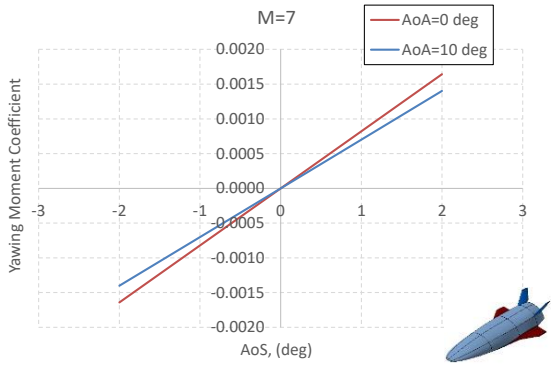

Fig 19. $C_{n\beta}$ for M_∞=7 and MRC at 45% L_{ref}.

The effect of elevon deflection on aircraft pitching moment is shown in Fig 20 for MRC at 45% L_{ref}. As shown, with MRC at 45% L_{ref}, allow trimming the aeroshape in the range 1÷7 deg AoA.

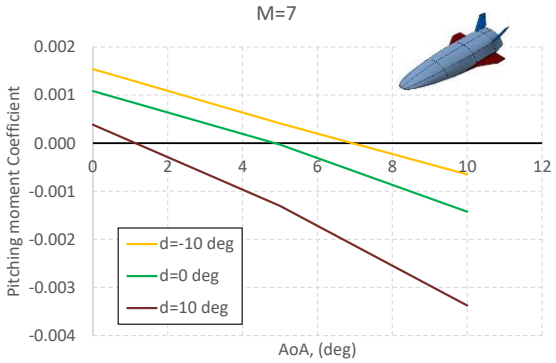

Fig 20. Control surface authority aerodynamics for M_∞=7 and -10°≤δ_{elevon}≤ 10°. MRC at 45% L_{ref}.

3.2. Low Speed Aerodynamics

To understand the aerodynamic performance and static stability at low speed, a combination of wind tunnel tests and CFD was completed. Analysis for this phase of flight will be crucial for landing and complete recovery of the vehicle. The subsonic investigations refer to a campaign analyzing the vehicle at V_∞=30 m/s for a Reynolds number of 1.35×10^6. This condition was chosen as it could be easily replicated in the wind tunnel.

Fig 21 shows a comparison of CFD and WT results for lift, drag, aerodynamic efficiency, and pitching moment coefficients. As with the high-speed analysis, the MRC was considered at 85% of the body length. Lift coefficient features a mostly linear lift curve slope and peak aerodynamic efficiency is found at 10 degrees AoA, with an L/D of approximately 5. No clear stall was identified from the CFD or the tunnel data and this behaviour is a characteristic of bodies which feature delta wing planforms and is expected by aeroshape designers. Generally, no difference between the structured mesh and the

unstructured mesh was observed, so the unstructured mesh was used for the remainder of the simulations due to meshing simplicity, particularly for the control deflection cases.

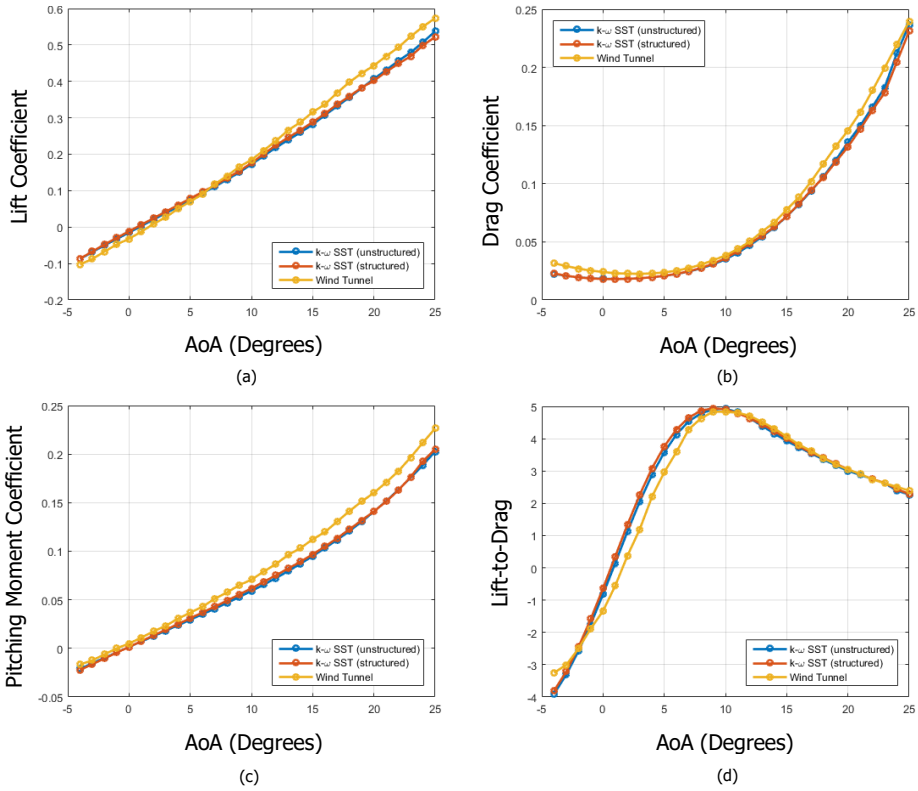

Fig 21. Wind Tunnel vs CFD results for (a) lift, (b) drag, (c) pitching moment and (d) L/D coefficients vs AoA with MRC at 85% L_{ref}.

To understand the flow features which govern the aerodynamic results gathered, images at increasing AoA were analysed and are presented in Fig 22. The development of vortices on the body of the vehicle with increasing AoA would explain the slight non-linearity in the lift curve slope and pitching moment results. It is also obvious that only weak leading-edge flow separation can be seen on the delta wing which is due to the rounded wing profile.

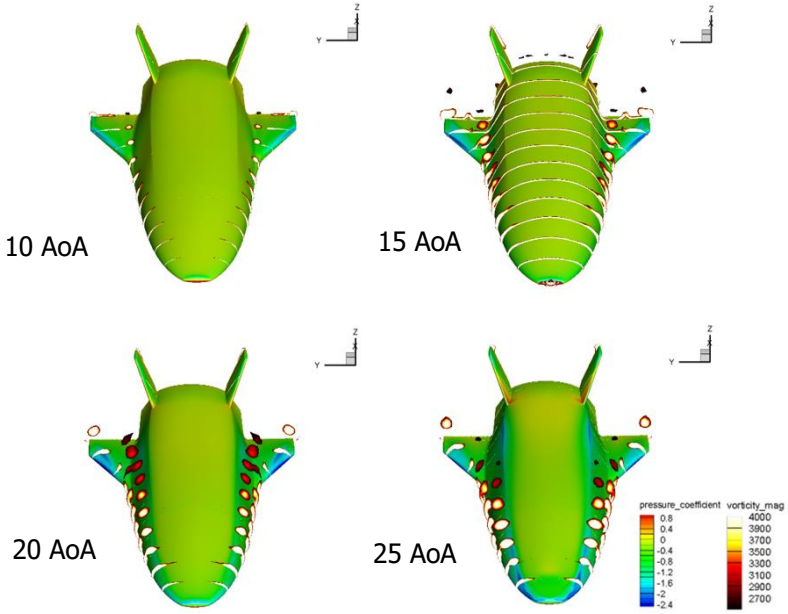

Fig 22. Formation of body vortices at increasing AoA.

As seen in the high-speed studies with the MRC located aft, the pitching moment coefficient has a positive gradient signifying instability. A study on MRC location and static longitudinal stability was performed for the same MRC locations presented in section 3.1 and the results shown in Fig 23. Each of these new MRC locations provide a negative gradient up to approximately 20 degrees AoA, meaning all configurations are stable up to this point. The non-linearity at high AoA is expected to be caused by the growth in forebody vortex strength with increasing AoA. The low speed stability analysis therefore agrees with a new MRC location at 45% of L_{ref} and will be used for all further analysis. One condition is that the vehicle landing speed needs to be high enough to avoid AoAs higher than 20 degrees.

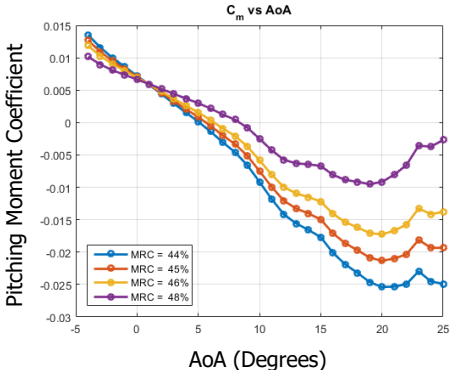

Fig 23. CFD pitching moment results for varying MRC location.

Fig 24 shows results from CFD elevon deflection studies. The results follow the expected trends, with downward deflections resulting in increased lift and drag. The graphs of lift-to-drag ratio show no significant impact on the maximum aerodynamic efficiency, but show a shift in location of the maximum value along the AoA axis. The zero degree deflection configuration has the highest lift-to-drag ratio of the five cases tested. The separation between lift and pitching moment plots show sufficient control authority.

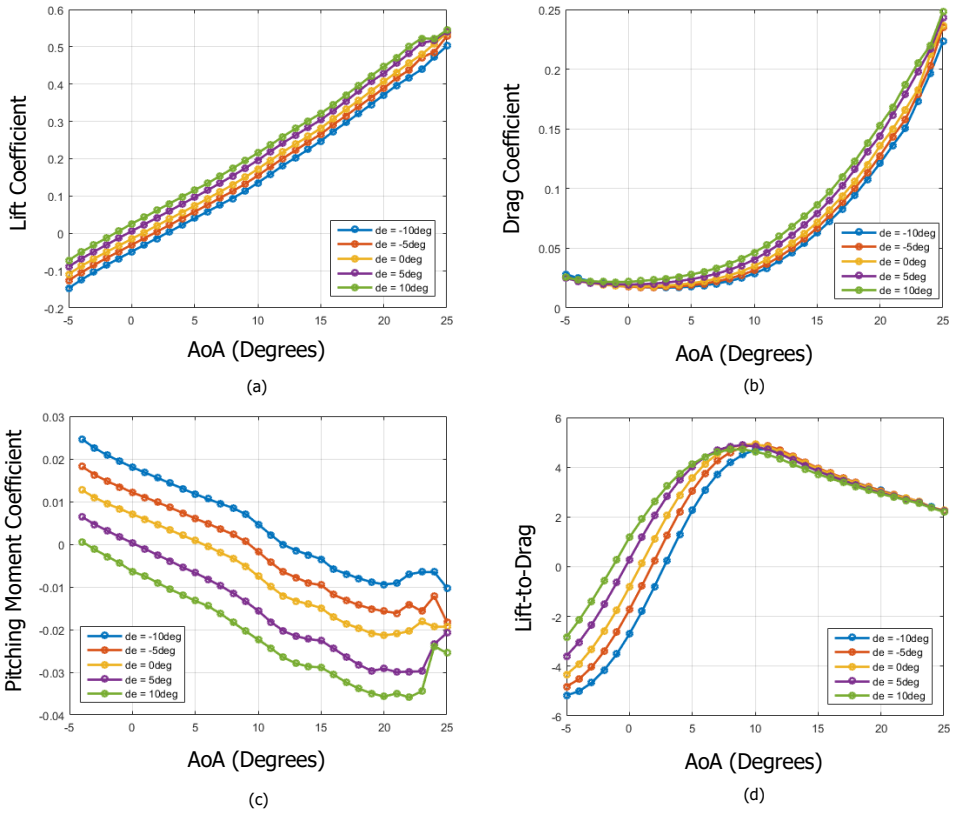

Fig 24. CFD results for (a) lift, (b) drag, (c) pitching moment and (d) L/D coefficients vs AoA with varying elevon deflection angles and MRC at 45% L_{ref}.

It is also interesting to note the sudden drop in lift at 24 degrees AoA for the positive elevon positions, with the maximum lift coefficient not improved upon when comparing with the 0 degree case. Further investigation found separation caused by the elevons and this is clearly seen in Fig 25. With reference to the free-stream velocity of 30m/s, the velocity magnitude with the elevon deflected at 10 degrees sees some velocity drop below 0m/s, indicating a region of separated, turbulent flow.

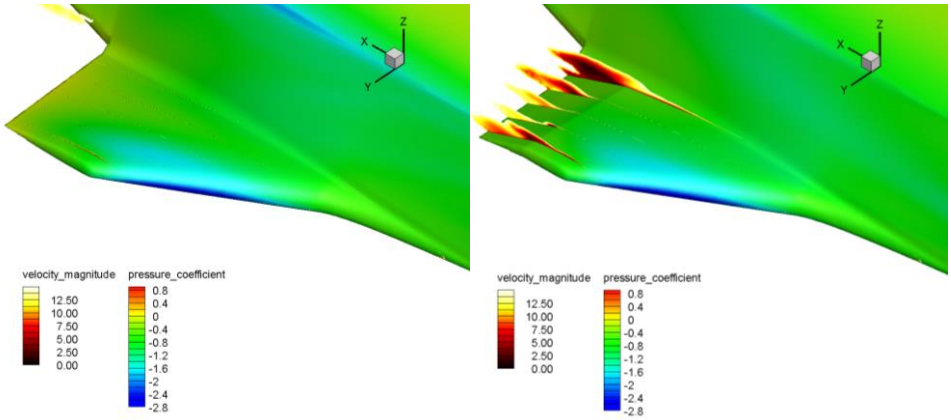

Fig 25. CFD images showing separation at elevon at 25 degrees AoA and δ_{elevon} = 0 and 10 degrees

For lateral/directional stability cases, the aircraft was subjected to varying side-slip angle and the results for rolling and yawing moment as well as side force were recorded. Fig 26 and Fig 27 show a comparison of wind tunnel data with CFD results at an AoA of 5 degrees. The experimental data compares well with numerical results, with the same trend/gradient for yawing moment and side force. Rolling moment shows a slight under prediction in gradient, but shows the same trend. Naturally, experimental measurements have offsets due to minor asymmetries in model and possible interference effects with the sting, but for stability prediction, the gradients are the parameters of interest, so these can also be neglected.

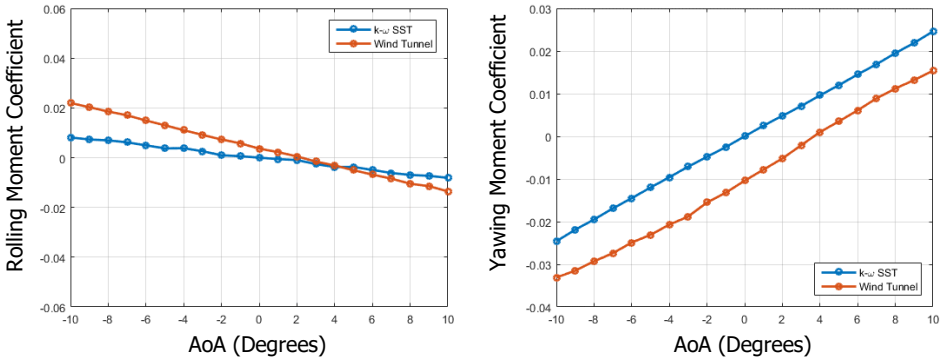

Fig 26. Comparison of CFD and wind tunnel results for (a) roll moment coefficient (b) yaw moment coefficient at MRC = 45% L_{ref}.

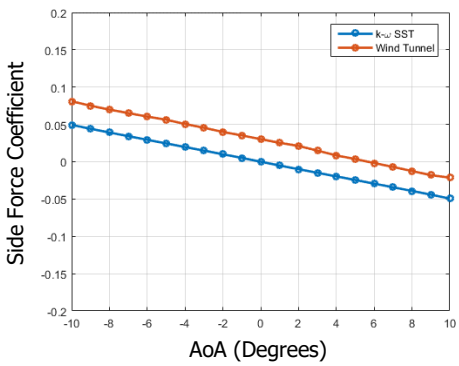

Fig 27. Comparison of CFD and wind tunnel results for side force coefficient.

Fig 28 shows instability in rolling moment at low AoA and stability in yaw through the AoA entire range.

During the descent and landing phase, the aircraft will need a high attitude angle to generate sufficient lift, so the roll instability at AoA below 0 AoA is not expected to impact aircraft controlability.

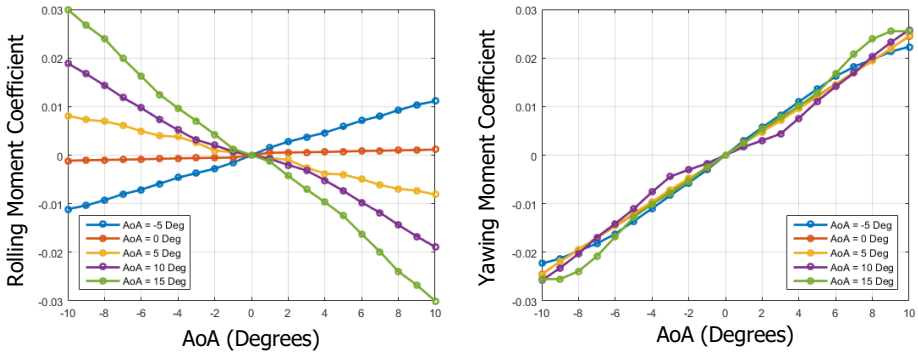

Fig 28. CFD results for roll and yaw moment coefficient at MRC = 45% L_{ref}.

The variance in side force coefficient with side-slip angle is presented in Fig 29. The negative gradient shows a stabilising force, demonstrating fin effectiveness. Some plateauing of the side force is seen at high AoA and high AoS,

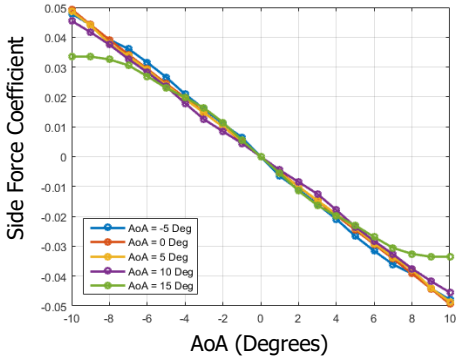

Fig 29. CFD results for side force coefficient.

Finally, Fig 30 shows the development of both asymmetric vortices and asymmetric wing pressure coefficients with increasing AoA at a constant 10 degrees AoS.

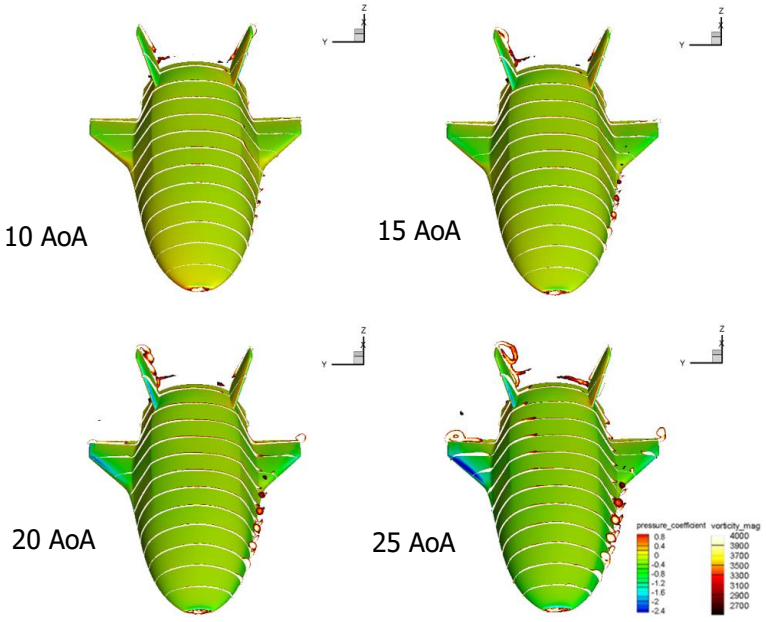

Fig 30. Asymmetric vortex development at increasing AoA, 10 degrees AoS.

The vortices originate mostly from the forebody as was seen in the longitudinal cases. It is clear that these vortices increase in strength with AoA and are a potential explanation for the reduction in yawing moment effectiveness at high AoA and AoS.

4. Conclusions

Re-usable, unmanned high-speed vehicles are an efficient way to experimentally validate next generation re-entry technologies. During the descent phase, the aircraft shall encounter different flow regimes ranging from hypersonic to low subsonic and this requires a careful aeroshape design. The success of a mission demands an aerodynamically stable vehicle during both the high-speed and low-speed re-entry flight. In this framework, this paper focused attention on both experimental and numerical flowfield investigations carried out on an innovative, spatuled-body aeroshape. Wind tunnel data was compared with CFD simulations to assess the low-speed performance of the aeroshape. For high-speed flow conditions, only CFD analyses are carried out so far.

Initial findings for the hypersonic speed conditions point out that the high streamlined sharp leading edges of the V-one configuration lead to a rather low wave drag component. However, aircraft leading edges feature thermo-mechanical load overshoots. Vehicle aerodynamics feature non-linear behavior, as expected for the hypersonic speed flow conditions. The peak aerodynamic efficiency of about 2.5 is attained at approximately 10 degrees AoA. In particular, a statically stable configuration in both longitudinal and lateral-directional flight conditions demands a very forward MRC position. Finally, the current sized elevon features a sufficient control authority.

Low speed aerodynamic analyses show that the lift coefficient features a mostly linear lift curve slope as expected for this flow regime and wing profile. The rounded leading edges of the double-delta planform prevent the formation of strong vortices, which would otherwise result in sharp changes in lift curve slope at high AoA. Vortices were instead observed forming along the forebody of the aircraft, which would contribute to aerodynamic forces and stability. Peak aerodynamic efficiency is found at about 10 degrees angle of attack, with a lift-to-drag ratio of approximately 5.

Similar to findings for the high-speed analysis, the original aft MRC location resulted in static instability for yaw and pitch. Static stability was achieved for most cases at the MRC suggested at the hypersonic analysis point, but was not achieved at AoAs below 0 for rolling moment. While undesirable, it is expected that the vehicle will be at high AoA during the descent and landing phase and is not deemed a critical issue. A good correlation between numerical and experimental data exists, particularly for the longitudinal studies and that numerical simulations were a good indicator of stability when compared with the wind tunnel data. A comparison of a structured domain with an unstructured showed little difference in extracted coefficients.

Future work on this aircraft will look at lateral/directional control through asymmetric elevon and ruddervator deflections, as well as analysis at more flight speeds.

References

1. Pezzella, G., Grardi, R., Guidotti G., Richiello, C., Aerodynamic and Aerothermodynamic Trade-off Analysis of the USV2 Flying Test Bed in the Framework of a Hypersonic Flight Test. 3rd International ARA Days. 2-4 May 2011. Archachon. France. AA-1-2011-54.
2. Pezzella, G., Richiello, C., Russo, G., Assessment of the Aerodynamic and Aerothermodynamic Performance of the USV-3 High-Lift Re-entry Vehicle. 7th European Symposium on Aerothermodynamics for Space Vehicles. European Space Agency (ESA). 9-12 May 2011. Site Oud Sint-Jan, Brugge. Belgium.
3. Scigliano, R., Pezzella, G., Di Benedetto, S., Marini, M., Steelant, J., "Hexafly-Int Experimental Flight Test Vehicle (EFTV) Aero-Thermal Design". Proceedings of the ASME 2017 International Mechanical Engineering Congress & Exposition IMECE 2017. November 3-9, 2017, Tampa, Florida, USA. ASME 2017 International Mechanical Engineering Congress and Exposition Volume 1: Advances in Aerospace Technology Tampa, Florida, USA, November 3–9, 2017.Conference Sponsors: ASME. ISBN: 978-0-7918-5834-9. Paper No. IMECE2017-70392, pp. V001T03A022; 14 pages doi:10.1115/IMECE2017-70392